Disproportionation of H2O2 to Dioxygen on a Nonheme Iron Center. A Computational Study

DOI:
10.1002/cctc.202300957

Document Version
Accepted author manuscript

RESEARCH ARTICLE

Disproportionation of H_2O_2 to Dioxygen on a Nonheme Iron Center. A Computational Study

Henrik P. H. Wong,[a,b] Frédéric Banse,[c] and Sam P. de Visser*[a,b]

[a] Mr. H.P.H. Wong, Dr S.P. de Visser
Manchester Institute of Biotechnology
The University of Manchester
131 Princess Street, Manchester M1 7DN, United Kingdom
E-mail: sam.devisser@manchester.ac.uk
URL: https://research.manchester.ac.uk/en/persons/sam.devisser

[b] Mr H.P.H. Wong, Dr. S. P. de Visser
Department of Chemical Engineering
The University of Manchester
Oxford Road, Manchester M13 9PL, United Kingdom

[c] Prof. F. Banse
Institut de Chimie Moléculaire et des Matériaux d'Orsay, CNRS
Université Paris-Saclay
91400, Orsay, France

Supporting information for this article is given via a link at the end of the document.

Abstract: Hydrogen peroxide is a versatile reductant that under the right conditions can react to form dioxygen in an electrochemical reaction. This reaction has a low carbon footprint and applications are being sought for batteries. In this work a computational study is presented on a recently reported nonheme iron(II) complex and study mechanistic pathways leading to dioxygen formation from H_2O_2. The work shows that upon reduction of the iron(III)-hydroperoxo species it rapidly leads through heterolytic cleavage of the dioxygen bond to form iron(IV)-oxo(hydroxo). The dimerization reaction of two iron(IV)-oxo(hydroxo) complexes then leads to formation of the dioxygen bond rapidly with small barriers. Dissociation of the dimer expels dioxygen in an exothermic reaction. We also tested an alternative mechanism through the formation of a μ-1,2-peroxo-μ-1,1-hydroperoxodiiron(II) intermediate but find the mechanism to be highly endergonic. These studies highlight the electrochemical feasibilities of nonheme iron(III)-hydroperoxo complexes.

Introduction

There are various mononuclear metalloenzymes in nature that utilize hydrogen peroxide as an oxidant for biochemical reaction processes related to biosynthesis and biodegradation. Thus, heme peroxidases bind H_2O_2 and through a machinery of electron and proton transfer steps detoxify it to two water molecules.[1] In addition, there are also enzymes in nature that can catalyze the conversion of hydrogen peroxide into dioxygen through a catalase process.[2] Catalases are heme enzymes with a tyrosinate axial ligand that take two molecules of H_2O_2 in their catalytic cycle. The first one of those is reduced to Compound I, i.e. the iron(IV)-oxo heme cation radical species, while a second H_2O_2 molecule leads to water and molecular oxygen as products. Hydrogen peroxide is an environmentally benign oxidant with a low carbon footprint and hence its use for oxidation reactions is well developed.[3] On the other hand, an electrochemical reaction can also lead to dioxygen formation and understanding and improving its use in batteries is of great scientific and environmental importance.[4]

To understand enzymatic reactivity and mechanisms, for many systems biomimetic models have been created.[5] These biomimetic models investigate the first- and second-coordination sphere effects of metal centers on reaction mechanisms and spectroscopic properties and help to understand enzymatic reactivity. Thus, reaction of excess H_2O_2 with an iron(II) complex often results in the formation of an iron(III)-hydroperoxo intermediate. Work on nonheme iron(III)-hydroperoxo complexes is well documented and these complexes have been trapped and characterized for a range of ligand systems.[6] Although, experimental work on heme and porphyrinoid iron(III)-hydroperoxo complexes failed to observe reactivity patterns with halides, sulfides and aromatic compounds, interestingly the nonheme iron(III)-hydroperoxo has been shown to efficiently react with these substrates.[7] Computational studies proposed the difference in reactivity of heme and nonheme iron(III)-hydroperoxo to be due to differences in O–OH cleavage patterns, whereby heme enzymes typically give heterolytic cleavage and the formation of OH^-, while nonheme iron(III)-hydroperoxo gives homolytic cleavage and an OH radical instead.[8]

To further establish the catalytic and electrochemical potential of nonheme iron(III)-hydroperoxo complexes, some of us recently described the synthesis and characterization of a nonheme iron(III)-hydroperoxo complex with *N*-methyl-*N*,*N*',*N*'-tris(2-pyridylmethyl)ethane-1,2-diamine) (L_5^2) ligand system, i.e. $[Fe^{III}(OOH)(L_5^2)]^{2+}$ designated **A** in Scheme 1.[9]

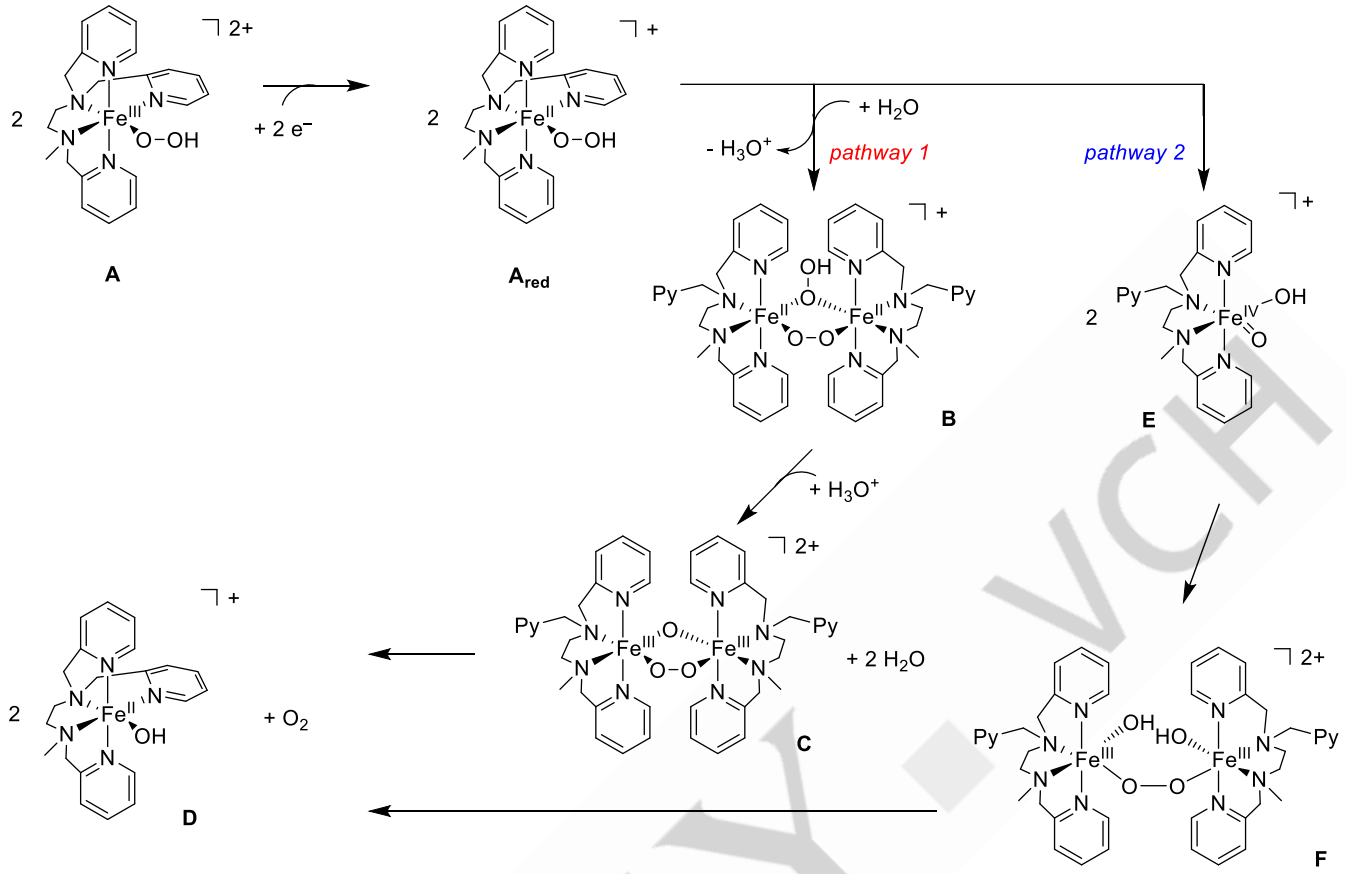

Scheme 1. Two suggested reaction pathways (1 and 2) for H_2O_2 conversion to dioxygen on a nonheme iron center explored in this work.

The complex was formed from the reaction of $[Fe^{II}Cl(L_5^2)](PF_6)$ with H_2O_2 in methanol and the resulting iron(III)-hydroperoxo species was characterized by UV-Vis spectroscopy and electron paramagnetic resonance (EPR) spectrometry studies as a doublet spin ground state. Cyclic voltammogram experiments in butyronitrile solvent revealed a cationic peak at $E_{p,c}$ = –0.20 V vs SCE for the reduction of **A** to $\mathbf{A}_{red}$. In addition, the cyclic voltammogram studies provided evidence of the formation of dioxygen dependent on the concentration of **A**, with the concomitant production of $[Fe^{II}(OH)(L_5^2)]^+$.

The experimental work established a reaction stoichiometry where two molecules of iron(III)-hydroperoxo reacted to form one molecule of dioxygen.[9] Previous calculations on Fenton type reactivity for the reaction of H_2O_2 on an iron(II) complex to form O_2, by contrast, predicted a 1:1 stoichiometry instead and the involvement of multiple H_2O_2 molecules in the process.[10] Therefore, the system described in this work is likely to undergo a different mechanism. Two possible reaction mechanisms for the disproportionation of the hydroperoxo ligand of reduced **A** in O_2 and hydroxide (*i.e.* iron(II)-hydroxo complex **D**) were suggested as displayed in Scheme 1 designated pathways 1 and 2. The first proposed pathway includes bridged peroxo and hydroperoxo diiron complexes, whereby two ions of $\mathbf{A}_{red}$ dimerize by expulsion of a proton to form the μ-1,2-peroxo-μ-1,1-hydroperoxo-diiron(II) complex **B** that reacts with H_3O^+ to form the μ-oxo-μ-1,2-peroxo-diiron(III) complex **C**. Structure **C** is proposed to react with a water molecule and release dioxygen and split into two mononuclear iron(II)-hydroxo complexes **D**. The alternative mechanism would start with heterolytic O–O cleavage of iron(II)-hydroperoxo ($\mathbf{A}_{red}$) to iron(IV)-oxo(hydroxo) complexes (**E**), which dimerize to form the μ-1,2-peroxo-diron(III)-dihydroxo complex (**F**). The latter can split off dioxygen and give two iron(II)-hydroxo complexes **D**. As experimental work failed to distinguish between these two possible reaction processes and find improvements of the disproportionation reaction for efficient H_2O_2 conversion into dioxygen, we decided to do a computational study to gain insight into the reaction pathways shown in Scheme 1. The work shows an efficient and highly exergonic pathway via the formation of structure **F**, while the hydroperoxo bridged dimer **B** is high in energy. Our studies identify the slowest and fastest steps in the dioxygen production reaction and may help to further develop novel catalysts for H_2O_2 redox chemistry.

Results and Discussion

Model validation.

Before testing the two catalytic mechanisms through pathways 1 and 2, we started the work with validating our computational methods and approaches against experimental data.

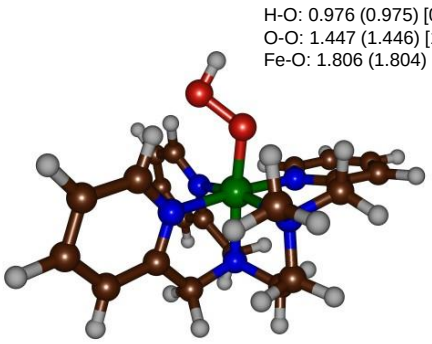

Fe-N_{ax}: 2.066 (2.059) [2.045]

$^{2}\mathbf{A}_{B3LYP}$ ($^{2}\mathbf{A}_{B3LYP\text{-}D3}$) [$^{2}\mathbf{A}_{PBE0}$]

	B3LYP	B3LYP-D3	PBE0
ΔE_{DQ}	3.2	7.3	3.0
ΔE_{DS}	3.5	4.7	4.2
$E°_{red}$ vs SCE	–0.23	–0.23	–0.23

^{4}A	B3LYP	B3LYP-D3	PBE0
Fe-N_{ax}	2.111	2.096	2.087
H-O	0.978	0.977	0.975
O-O	1.430	1.433	1.402
Fe-O	1.809	1.803	1.802

^{6}A	B3LYP	B3LYP-D3	PBE0
Fe-N_{ax}	2.271	2.270	2.246
H-O	0.977	0.977	0.974
O-O	1.419	1.421	1.399
Fe-O	1.873	1.867	1.857

Figure 1. DFT optimized geometries of $^{2,4,6}[Fe^{III}(OOH)(L_5{}^2)]^{2+}$ (^{2,4,6}**A**) calculated using different DFT approaches. Bond lengths are in angstroms, doublet-quartet energy spitting (ΔE_{DQ}) and doublet-sextet energy splitting (ΔE_{DS}) are ΔE+ZPE values calculated at BS2//BS1 in kcal mol^{-1}. The reduction potential ($E°_{red}$) is in V and relative to SCE.

The iron(III)-hydroperoxo complex (**A**) was, therefore, geometry optimized in the lowest energy doublet, quartet and sextet spin states using the B3LYP, B3LYP-D3 and PBE0 approaches, see Figure 1. We then calculated the adiabatic spin state energies for the adiabatic doublet-quartet (ΔE_{DQ}) and doublet-sextet (ΔE_{DS}) energy gaps using basis set BS2 calculated energies and basis set BS1 calculated zero-point energies (ZPE) at ΔE+ZPE level of theory. Free energies (ΔG) were obtained by correcting these ΔE+ZPE values with thermal and entropic corrections at 298 K. Using all methods the doublet spin state is the ground state in agreement with experimental electron paramagnetic resonance (EPR) data that characterized **A** as a doublet spin ground state. With the B3LYP approach the quartet and sextet spin states of structure **A** are higher in energy by 3.2 and 3.5 kcal mol^{-1}, while dispersion corrections widens these energy gaps to 7.3 and 4.7 kcal mol^{-1}. With PBE0 similar energetics is obtained as with B3LYP that put the quartet and sextet spin states above the doublet state by 3.0 and 4.2 kcal mol^{-1}, respectively. Nevertheless, it is clear that the three spin states are close in energy and may scramble during the reaction mechanism. The doublet spin state has orbital occupation $\pi^*_{xy}{}^2\ \pi^*_{xz}{}^2\ \pi^*_{yz}{}^1$ and as a result the unpaired spin density is dominant on the iron atom.

Optimized geometries are shown in Figure 1 for the doublet spin state structures as calculated with the three density functional theory (DFT) methods. In general, the structures resemble previous calculations on nonheme iron(III)-hydroperoxo structures well.[8,10,11] As can be seen, optimized geometries have most distances within 0.010 Å and hence little variation is observed when the computational method or approach is changed. In particular, the Fe–O and Fe–N_{ax} distances, where N_{ax} is the axial nitrogen atom trans to the oxygen atom, are within narrow windows of 1.796 – 1.806 Å and 2.045 – 2.066 Å, respectively. A bit larger fluctuation is seen for the O–O interaction with distances that range from 1.422 – 1.447 Å. Weak hydrogen bonding interactions from pyridine hydrogen atoms to the oxygen atoms of the hydroperoxo group stabilize the structure.

To further validate our approaches we calculated the adiabatic reduction potential ($E°_{red}$) of ^{2}**A** using all three DFT approaches to form $\mathbf{A}_{red}$ through full geometry optimizations for all possible spin states at B3LYP, B3LYP-D3 and PBE0 level of theory. With all three methods the reduced state $\mathbf{A}_{red}$ is in a quintet spin ground state that is more than 5 kcal mol^{-1} lower in energy than the alternative singlet and triplet spin states (see Supporting Information). Interestingly, regardless of the computational method, the energy difference between the lowest energy **A** and $\mathbf{A}_{red}$ structures is very similar and a reduction potential of –0.23 V vs SCE is obtained with the all three DFT methods. These values are in excellent agreement with the experimentally obtained value of –0.20 V.[9] Overall, therefore, the calculations do not appear to fluctuate much with the choice of the density functional method used and all methods reproduce experimental data well.

Structurally, the $^{5}\mathbf{A}_{red}$ structures have an elongated Fe–O interaction that ranges between 1.940 – 1.960 Å for the three DFT methods, while the Fe–N_{ax} elongates to 2.345 – 2.390 Å. This is the result of single occupation of the antibonding σ^*_{z2} orbital along the O–Fe–N_{ax} axis. The overall configuration of $^{5}\mathbf{A}_{red}$ obtained with all three DFT approaches is a state with orbital occupation $\pi^*_{xy}{}^2\ \pi^*_{xz}{}^1\ \pi^*_{yz}{}^1\ \sigma^*_{z2}{}^1\ \sigma^*_{x2\text{-}y2}{}^1$. As a result, the adiabatic reduction of **A** to

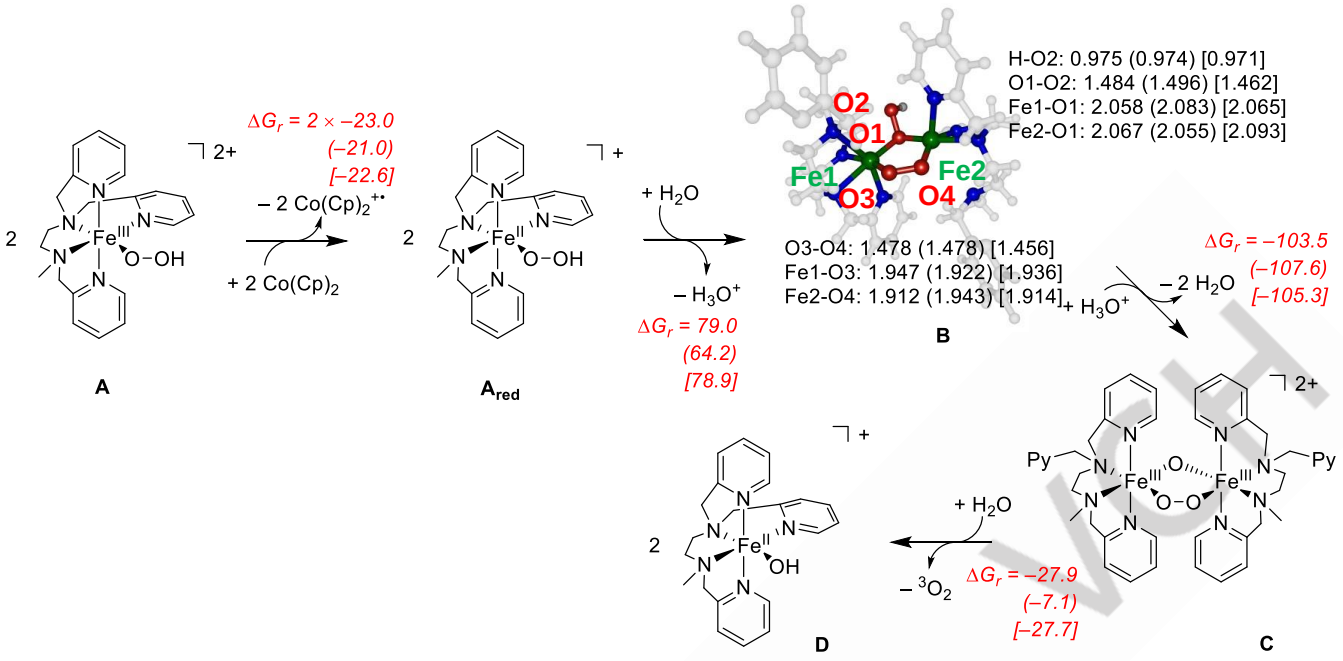

Figure 2. Reaction free energies for individual steps for pathway 1 calculated with energies at BS2 level of theory and zero-point, thermal and entropic corrections at BS1 level of theory. Free energies are in kcal mol^{-1} for the designated reaction steps calculated using different DFT approaches: B3LYP (data out of parenthesis), B3LYP-D3 (data in parenthesis) and PBE0 (data in square brackets). DFT optimized geometries of $^{9}[Fe^{II}_2(OOH)(O_2)(L_5^2)_2]^+$ (^{9}**B**) have bond lengths in angstroms.

A$_{red}$ leads to a double electron transfer where one electron from π^*_{xz} is promoted to $\sigma^*_{z^2}$ and the incoming electron fills the $\sigma^*_{x^2-y^2}$ orbital. The O–O bond is slightly elongated to 1.452 – 1.482 Å. The structure, spin state ordering and electronic configuration of **A**$_{red}$ compares well to alternative iron(III)-hydroperoxo and iron(III)-hydroperoxo structures from the literature.[10,11]

Pathway 1 reaction mechanism.

Subsequently, we focused on the reaction mechanism for conversion of the iron(III)-hydroperoxo complex into dioxygen and an iron(II)-hydroxo species and considered the possible pathways 1 and 2 as described above in Scheme 1. Let us start with pathway 1 and the reaction energies for each step are shown in Figure 2. We again ran full geometry optimizations in all possible spin states for each intermediate and calculated reaction energies for each step in the mechanism using B3LYP, B3LYP-D3 and PBE0. In general, irrespective of the computational method, the same pattern and trends are seen leading to the same conclusions. Thus, the reduction free energy of the iron(III)-hydroperoxo species to form the iron(II)-hydroperoxo complex using the $Co(Cp)_2/Co(Cp)_2^{+\bullet}$ couple is exergonic by ΔG = –23.0 (B3LYP), –21.0 (B3LYP-D3) or –22.6 (PBE0) kcal mol^{-1}. Clearly the various methods give similar trends in reaction patterns.

To estimate the electron transfer rate for the reaction of **A** with cobaltocene we used Marcus theory to determine the free energy of activation of the electron transfer reaction, see Methods and Supporting Information for details. At UB3LYP level of theory we calculate a reaction free energy for the reduction of **A** to **A**$_{red}$ of ΔG_r = –23.0 kcal mol^{-1}, which corresponds to an electron transfer free energy of activation for the conversion of **A** to **A**$_{red}$ by $Co(Cp)_2$ of $\Delta G^{\ddagger}_{A\text{->}Ared}$ = 5.4 kcal mol^{-1}. This is a very small barrier and implies a fast conversion of **A** to **A**$_{red}$ in the presence of cobaltocene as a reducing agent at room temperature. It has been anticipated that two iron(II)-hydroperoxo species (**A**$_{red}$) with assistance of a water molecule can form the μ-1,2-peroxo-μ-1,1-hydroperoxo-diiron(II) complex **B** upon release of a H_3O^+.[9] The optimized geometry of **B** was calculated with odd multiplicity and the structure lowest in energy is the nonet spin state at UB3LYP and B3LYP-D3 level of theory, while the septet spin states is lowest with PBE0. All other electronic states were also calculated but found to be >10 kcal mol^{-1} higher in energy than the ground state for all methods (see Supporting Information). Energetically, the formation of **B** from two molecules of **A**$_{red}$ and a water molecule is endergonic by ΔG_r = +79.0 kcal mol^{-1} at the UB3LYP/BS2//UB3LYP/BS1 level of theory, while with dispersion corrections it is of similar value at 64.2 kcal mol^{-1} and the PBE0 approach gives 78.9 kcal mol^{-1}. Therefore, it is clear that the formation of the μ-1,2-peroxo-μ-1,1-hydroperoxo diiron(II) complex is highly endergonic and consequently it is unlikely complex **B** will be formed under room temperature conditions from **A**$_{red}$. Optimized nonet spin geometries of **B** are shown in Figure 2. The B3LYP optimized structure of ^{9}**B** puts the two iron and three oxygen atoms in virtually the same plane, while the hydroxo group is displaced from the plane with a dihedral angle of 129 degrees. The peroxo group is stabilized through six weak hydrogen bonding interactions from methyl C–H groups of the ligand system. Optimized geometries with B3LYP, B3LYP-D3 and PBE0 are similar with an O-O distance ranging from 1.456 – 1.478 Å, while

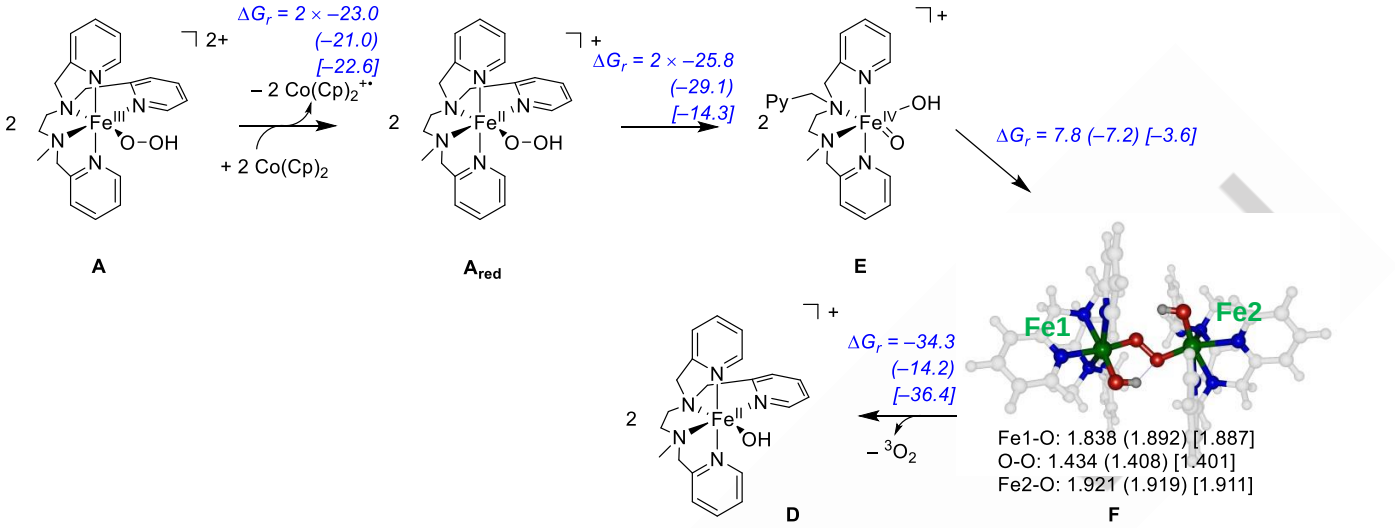

Figure 3. Reaction free energies for individual steps calculated for pathway 2 at UB3LYP/BS2 level of theory with zero-point, thermal and entropic corrections at UB3LYP/BS1. Free energies are in kcal mol^{-1} for the designated reaction steps. DFT optimized geometries of $[Fe^{III}_2(OH)_2(O_2)(L_5^2)_2]^+$ (**F**) calculated using different DFT approaches: B3LYP (^{9}**F**, data out of parenthesis), B3LYP-D3 (^{11}**F**, data in parenthesis) and PBE0 (^{11}**F**, data in square brackets). Bond lengths are in angstroms.

the Fe–O interactions to the peroxo group are from 1.912 – 1.947 Å. The hydroperoxo binding also shows similar geometric features between the three DFT methods with Fe–O distances longer than 2 Å for all methods and an O–OH distance similar to the mononuclear iron-hydroperoxo complexes discussed above. Thereafter, the OH^- transfer from complex **B** to a H_3O^+ gives the μ-1,2-peroxo-μ-oxodiiron(III) intermediate **C**. These μ-1,2-peroxo-μ-oxodiiron intermediates are common intermediates in diiron enzymes and have, e.g., been characterized for ribonucleotide reductase and Δ^9-stearoyl-acyl carrier protein desaturase.[12] Energetically, the formation of **C** and two water molecules from the reaction of **B** with H_3O^+ is exergonic by ΔG = –103.5 kcal mol^{-1} at B3LYP level of theory, while with B3LYP-D3 and PBE0 the free energy changes are –107.6 and –105.3 kcal mol^{-1}, respectively. Complex **C** is in an undecaplet spin ground state with five ferromagnetically coupled metal-based electrons on each iron center. Geometrically structure **C** has the oxo group midway in between the two iron atoms at distances of 1.858 and 1.859 Å. The peroxo bond is 1.428 Å and its distances to the two iron atoms are 1.918 and 1.921 Å. Furthermore, the μ-oxo-μ-peroxo diiron structure is close to planarity. A transition state designated $\mathbf{TS}_{BC}$ was located for the O–OH bond cleavage of the hydroperoxo group in **B** to form the μ-1,2-peroxo-μ-oxodiiron(III) complex **C**. Energetically it is ΔG = 4.2 kcal mol^{-1} higher in energy than structure **B** with an imaginary frequency of 649 cm^{-1} representing the O–OH stretch vibration, see Supporting Information Figure S1. Release of dioxygen from complex **C** and a water molecule gives two mononuclear iron(II)-hydroxo (**D**) complexes at the expense of ΔG = –27.9 (B3LYP), –7.1 (B3LYP-D3) and –27.7 (PBE0) kcal mol^{-1}. Similarly to the iron(II)-hydroperoxo complexes also the iron(II)-hydroxo complexes are in a high-spin ground state. With all DFT approaches the quintet spin ground state of **D** is more than 10 kcal mol^{-1} separated from the lowest energy singlet and triplet spin states. The Fe–O and Fe–N_{ax} distances; however, are significantly longer for ^{5}**D** as compared to $^5\mathbf{A}_{red}$. For instance the B3LYP optimized structures have Fe–O and Fe–N_{ax} bond lengths of 1.923 and 2.402 Å, respectively.

In summary, pathway 1 contains one highly endergonic reaction step for the formation of structure **B** from two $\mathbf{A}_{red}$ ions, which is an amount of energy that the system may not have available at room temperature and will make pathway 1 an unlikely mechanism here.

Pathway 2 reaction mechanism.

Next, we explored the alternative mechanism via pathway 2 and the results of the reaction energies for each step are shown in Figure 3. The reaction similarly to the pathway from Figure 2 starts with the reduction of the iron(III)-hydroperoxo species to iron(II)-hydroperoxo. The iron(II)-hydroperoxo species through O–O cleavage forms an iron(IV)-oxo(hydroxo) intermediate in a heterolytic O–O cleavage step. The O–O cleavage is exergonic by ΔG = –25.8 (–29.1) [–14.3] kcal mol^{-1} as obtained at B3LYP (B3LYP-D3) and [PBE0] level of theory, respectively. Using B3LYP and PBE0 the structure remains a quintet spin ground state during the conversion from $\mathbf{A}_{red}$ to **E**; however, with B3LYP-D3 a lower energy triplet spin state is found. Thereafter, with B3LYP a small barrier and a small endergonic step of ΔG_r = 7.8 kcal mol^{-1} forms the μ-1,2-peroxo-bound diiron complex **F**, while

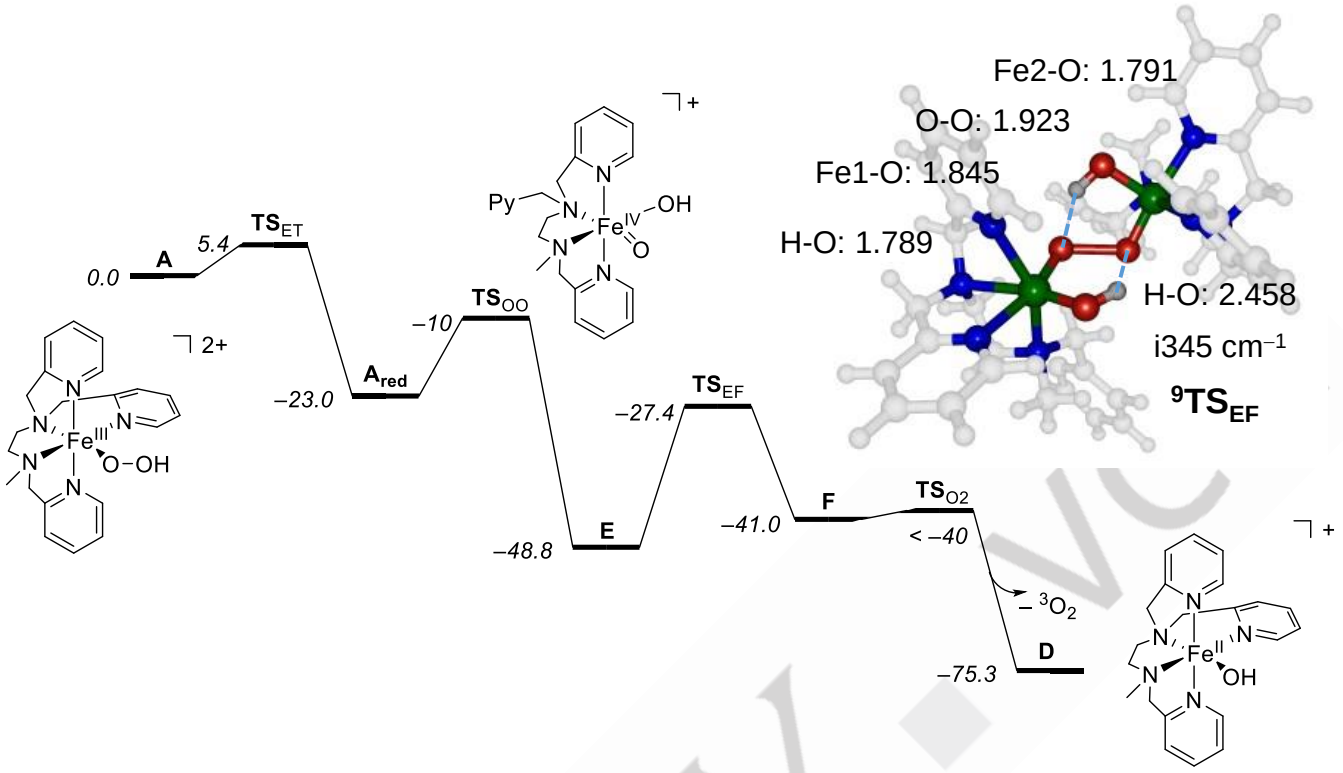

Figure 4. UB3LYP/BS2//UB3LYP/BS1 calculated potential energy landscape for pathway 2 reactivity as obtained in Gaussian-09. Optimized transition state geometry for the O–O bond formation to form **F** from two molecules of **E** is given with bond lengths in angstroms and the imaginary frequency in cm^{-1}. Free energies are given in kcal mol^{-1} and include solvent, entropic, zero-point and thermal corrections to the energy at 298 K.

with B3LYP-D3 and PBE0 the reactions are exergonic by –7.2 and –3.6 kcal mol^{-1}. Structure **F** can release $^3O_2$ and split into two iron(II)-hydroxo complex with an exergonic step of ΔG_r = –34.3 (B3LYP), –14.2 (B3LYP-D3) and –36.4 (PBE0) kcal mol^{-1}. As such the cycle in Figure 3 implicates a small energetic barrier for the formation of structure **F** but an overall highly exergonic reaction for conversion of hydrogen peroxide into dioxygen that should be feasible under room temperature conditions. The reaction step for the formation of a dioxygen bond from two metal-oxo complexes is reminiscent of the dioxygen bond formation in Nature by Photosystem II, where two high-valent manganese(V)-oxo species are involved.[13]

Optimized geometries of the lowest energy diiron complex **F** are shown in Figure 3. At UB3LYP level of theory the nonet spin state is lowest by ΔG = 2.4 and 2.3 kcal mol^{-1} over the undecaplet and open-shell singlet spin states, respectively, while the spin state ordering is reversed with the UB3LYP-D3 and PBE0 methods. Regardless of the method used; however, the open-shell singlet, nonet and undecaplet states are close in energy. Optimized geometries of ^{9}**F** (B3LYP) and ^{11}**F** (B3LYP-D3 and PBE0) are shown in Figure 3. All structures have a somewhat shorter Fe1–O distance than the Fe2–O distance by 0.024 – 0.083 Å, which implies that the two iron centers are unequal. This is most likely caused by the hydrogen bonding interactions of the two hydroxo groups in the structure that removes the symmetry. Thus, in the B3LYP structure bond hydroxo groups hydrogen bond with an oxygen atom of the peroxo group. By contrast in the PBE0 and B3LYP-D3 optimized structures one of the hydroxo groups hydrogen bonds to the oxygen atom of the other hydroxo group, while the peroxo group is not involved in direct hydrogen bonding interactions.

To gain insight into the kinetics of the reaction cycle, we decided to calculate key transition states for reaction steps in the mechanisms and particularly for steps related to pathway 2 and show the full potential energy profile in Figure 4. As mentioned above, the electron transfer free energy from cobaltocene to **A** has a free energy of activation of $\Delta G^{\ddagger}$ = 5.4 kcal mol^{-1} via transition state $\mathbf{TS}_{ET}$. This small barrier, implicates that the electron transfer will happen rapidly and will not be rate determining. Indeed the electron transfer is exergonic by 23.0 kcal mol^{-1}.

Subsequently, the iron(II)-hydroperoxo cleaves the O–O bond to form the iron(IV)(oxo)hydroxo complex **E**. Geometry scans were run on all spin state surfaces and showed a smooth energetic curve for O–O bond cleavage. Moreover, upon cleavage of the O–OH bond the released OH group binds iron and no free OH radicals are formed in the process. We attempted to locate a transition state for this step, and characterized it at about 13 kcal

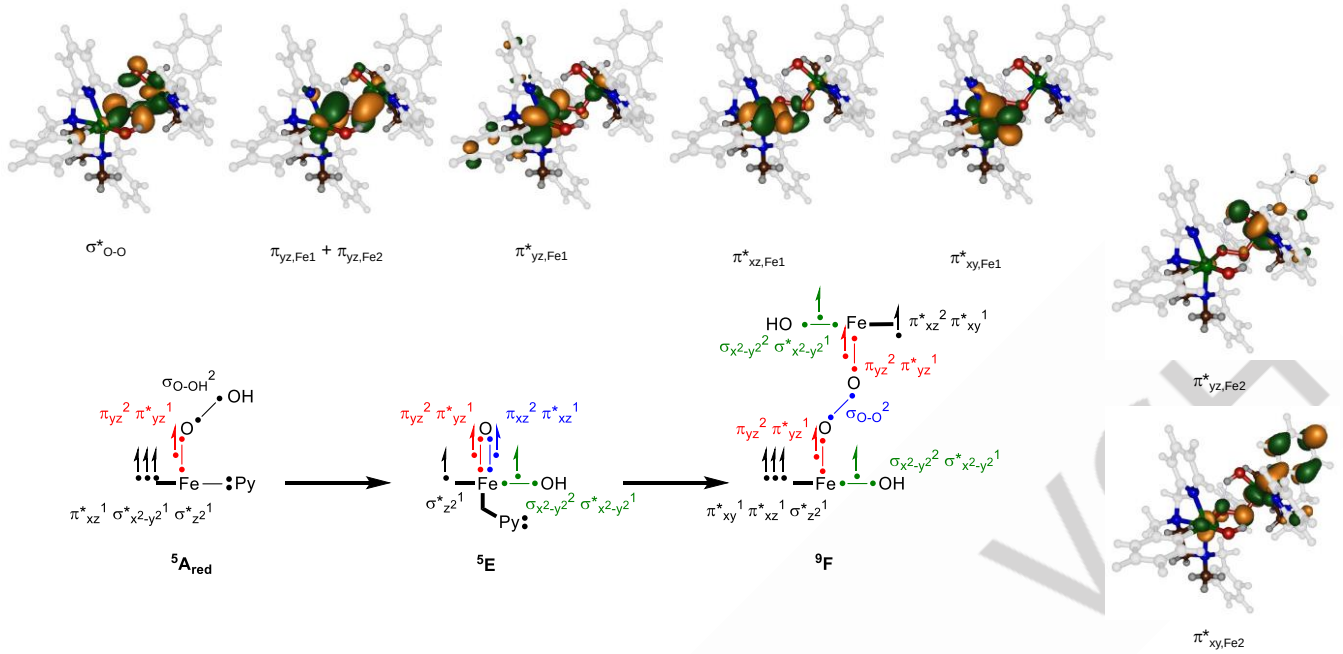

Figure 5. Valence bond description of bond and orbital changes for the pathway to form ^{9}**F** from ^{5}**A**$_{red}$. Dots represent an electron and a line separating two dots is a bond orbital occupied by two electrons. Unpaired electrons are highlighted with an arrow. Key valence orbitals of ^{9}**F** are shown.

mol^{-1} above the energy of ^{5}**A**$_{red}$. The reaction exergonicity from ^{5}**A**$_{red}$ to ^{5}**E** is high and releases 25.8 kcal mol^{-1}.

The only endergonic step in pathway 2 is the association of two iron(IV)-oxo(hydroxo) complexes **E** into a μ-peroxo-diiron(III)-dihydroxo complex **F**. Therefore, we searched for a transition state structure for this step on the lowest energy spin state surface, i.e. the nonet spin state. The optimized transition state for the step from **E** to **F** (**TS**$_{EF}$) is shown in Figure 4. We find a free energy of activation as calculated at UB3LYP/BS2//UB3LYP/BS1 level of theory with zero-point, entropic and thermal corrections included of 21.4 kcal mol^{-1} with respect to structure **E**. This is a relatively low free energy and implicates a possible reaction at room temperature and pressure.

The optimized ^{9}**TS**$_{EF}$ structure displayed in Figure 4 gives a long O–O distance of 1.923 Å, while the imaginary frequency of i345 cm^{-1} corresponds to an O–O stretch vibration. Therefore, the structure and imaginary frequency characterizes the transition state as an O–O formation barrier for the coupling of two iron(IV)-oxo(hydroxo) intermediates into a dimer. The two Fe–O bonds of the nascent peroxo bridge, surprisingly are unequal, i.e. Fe1–O is 1.845 Å and Fe2–O is 1.791 Å. This is probably the result from hydrogen bonding interactions of the hydroxo groups to the peroxo bridge, whereby one of these is particularly strong and short (1.789 Å hydrogen bond), while it is longer and therefore much weaker to the other oxygen atom (2.458 Å hydrogen bond). Both Fe–O bonds have elongated considerably from the distances seen in the isolated iron(IV)-oxo(hydroxo) complexes that have Fe=O distances of 1.633 Å at UB3LYP/BS1 level of theory in the quintet spin state and shown before on analogous iron(IV)-oxo, iron(IV)-oxo(hydroxo) complexes calculated before.[14] The elongated Fe–O distance in ^{9}**TS**$_{EF}$ as compared to ^{5}**E** is the result of an electron transfer from oxygen to iron that is reduced from iron(IV) to iron(III). The transition state gives a spin density of 0.29 on the oxo group of Fe1, while it is –0.25 on the other oxo group bound to Fe2. The spin densities, therefore, implicate an O–O bond formation step where a down-spin electron on atom O1 and an up-spin electron on atom O2 form a new covalent bond in the dimer complex. The final step for dioxygen release from **F** has a small barrier that we were unable to characterize but as the exothermicity for this step is very large, we assume the **TS** to be low in energy.

To understand the structure and stability of compound **F**, we analyzed the molecular orbitals of the lowest energy pathway 2 structures ^{5}**A**$_{red}$, ^{5}**E** and ^{9}**F**. Figure 5 shows key molecular orbitals of ^{9}**F** as well as valence bond (VB) descriptions of the electronic configurations of the complexes leading to ^{9}**F**. Thus, in VB theory a bonding orbital occupied with two electrons is described as a line with a dot at each end. In the iron(II)-hydroperoxo complex the metal forms chemical bonds with the ligand framework as well as the hydroperoxo group.[15] The Fe–O bond, however, is occupied with three electrons in the π_{yz} and π^*_{yz} orbitals, hence there are three dots representing three electrons in the VB diagram along the yz-axis (shown in red). Thus, two of these electrons fill the π_{yz} orbital while the antibonding orbital is singly occupied. As an antibonding orbital is occupied by one electron this leads to elongation of the Fe–O bond in the iron(II)-hydroperoxo species and consequently a relatively long distance of 1.8 Å is obtained. The hydroperoxo group has a $\sigma_{O\text{-}OH}$ orbital for the dioxygen interaction that is doubly occupied and therefore the bond orbital in the VB diagram has two electrons. The ^{5}**A**$_{red}$

structure also has three unpaired electrons in the π^*_{xz}, $\sigma^*_{x2\text{-}y2}$ and σ^*_{z2} molecular orbitals shown with a dot and single arrow in Figure 5. The π^*_{xz} orbital is in the plane of the FeOOH group and resembles the atomic $3d_{xz}$ iron-type orbital. The σ^*_{z2} is antibonding between the iron and oxygen atom, while the $\sigma^*_{x2\text{-}y2}$ orbital is antibonding between iron and ligand nitrogen atoms. The iron atom forms a dative bond with a pyridine (Py) group in the equatorial plane as identified with the two electrons closest to the Py group in Figure 5.

Upon conversion from $^5\mathbf{A}_{red}$ to $^5\mathbf{E}$, the dative bond between iron and Py is broken as well as the O–OH bond ($\sigma_{O\text{-}OH}$ orbital). At the same time the iron-OH bond is formed as a bonding orbital between the $2p_y$ atomic orbital on oxygen with the $3d_{x2\text{-}y2}$ orbital on iron in the xy-plane. Also an iron-oxo species results in two sets of two-center-three-electron bonds for the $\pi_{xz}^2\ \pi^*_{xz}{}^1$ interaction (shown in red) and for the $\pi_{yz}^2\ \pi^*_{yz}{}^1$ interaction (shown in blue). The two unpaired electrons along the Fe–O bond lead to considerable spin density on the oxygen atom, which indeed is 0.57 (B3LYP structure). The radical character of the oxygen atom enables the formation of a dioxygen bond during the collision of two iron(IV)-oxo(hydroxo) complexes to give dimer $^9\mathbf{F}$. Formation of $^9\mathbf{F}$ from two molecules of $^5\mathbf{E}$ results in the breaking of the two-center-three-electron bonds for both Fe–O groups in the xz-plane. The three electrons of those orbitals are redistributed over the complex and form the new O–O bond ($\sigma_{O\text{-}O}$), while one unpaired electron stays on each of the iron atoms in the π^*_{xy} and π^*_{xz} orbitals, although the spin is not equal on both iron atoms.

Conclusion

A series of computational studies on the reaction of H_2O_2 on an iron(II) center leading to dioxygen are presented. Several possible reaction pathways were studied via either a μ-1,2-peroxo-μ-1,1-hydroperoxo diiron(III) intermediate or a μ-1,2-peroxo diiron(III)dihydroxo complex. Full geometry optimizations in all possible spin states for all complexes were done using several DFT approaches. In general, the calculations give little variation upon changing the DFT method and give the same trends and conclusions. Overall, the lowest energy pathway appears to proceed through the dimerization of two iron(IV)-oxo(hydroxo) complexes to give a μ-1,2-peroxo diiron(III)-dihydroxo complex. A transition state was characterized for the step and identifies a free energy of activation of $\Delta G^{\ddagger}$ = 21.4 kcal mol^{-1} with respect to **E** as the rate-determining step in the reaction pathway and subsequently releases dioxygen. Overall the calculations show that the iron(II) complex could operate with H_2O_2 to form dioxygen products. The rate-determining step of the reaction, however, will be dependent on the concentration of the iron(IV)-oxo(hydroxo) intermediate and in a relatively high concentration should be able to form the dimer complex through formation of an O–O bond between the two oxo radicals. In contrast, a low concentration may help intercepting the iron(IV)-oxo(hydroxo) with a substrate in order to evaluate the oxidizing ability of such an uncommon intermediate.

Methods

All calculations were performed with the Gaussian-09 software package and utilize density functional theory (DFT) approaches.[16] Three DFT methods were tested for all structures, namely the unrestricted B3LYP,[17] B3LYP-D3,[17,18] PBE0 functionals.[19] Geometries were optimized (without constraints) with each of these DFT methods in combination with a basis set, designated BS1, that contains cc-pVTZ on iron and 6-31G* on the rest of the atoms.[20] These calculations included a continuous polarized conductor model with a dielectric constant mimicking butanonitrile.[21] Stationary points were calculated on all possible spin states, including the broken-symmetry singlet spin diiron complexes to obtain antiferromagnetically coupled states. Local minima were characterized with a frequency calculation that established real frequencies only. To improve the energetics single point calculations with a basis set, designated BS2, containing cc-pVTZ on iron and 6-311++G** on the rest of the atoms was applied. Reduction potentials were calculated from the adiabatic energy differences between the oxidized and reduced forms using basis set BS2. Reduction free energies were corrected with a value of –0.25 V to accommodate a measurement as compared to an SCE electrode.[22] The methods and computational approaches were extensively validated previously and found to reproduce experimental free energies of activation, experimental product distributions, reduction potentials and spectroscopic parameters well.[23]

Kinetics of electron transfer processes were calculated with respect to the cobaltocene/cobaltocenium couple using Marcus theory as described in Eq 1.[24] The electron transfer free energy of activation ($\Delta G^{\ddagger}_{ET}$) is determined by the electron transfer free energy (ΔG_r) and the reorganization energy λ. The reorganization energy was determined from the solvent and internal reorganization energies as described before.[24b,25]

$$\Delta G_{ET}^{\neq} = \frac{\lambda}{4}\left(1+\frac{\Delta G_r}{\lambda}\right)^2 \qquad (1)$$

Supporting Information

Supporting Information is provided with all raw data, including Cartesian coordinates of all optimized geometries, absolute and relative energies and tables with group spin densities and charges.

Acknowledgements

HPHW thanks the University of Manchester for a PGRTA studentship. The computational shared facilities (CSF) at the University of Manchester are thanked for providing CPU time for this project.

Keywords: biomimetic models • density functional theory • dioxygen • inorganic reaction mechanisms • nonheme

[1] a) M. Sono, M. P. Roach, E. D. Coulter, J. H. Dawson, *Chem. Rev*. **1996**, *96*, 2841–2887; b) Raven, *Nat. Prod. Rep*. **2003**, *20*, 367–381; c) T. L.

Poulos, *Arch. Biochem. Biophys*. **2010**, *500*, 3–12; d) A. O. Falade, U. U. Nwodo, B. C. Iweriebor, E. Green, L. V. Mabinya, A. I. Okoh, *Microbiol. Open* **2017**, *6*, e00394; e) M. Lučić, M. T. Wilson, D. A. Svistunenko, R. L. Owen, M. A. Hough, J. A. R. Worrall, *J. Biol. Inorg. Chem*. **2021**, *26*, 743–761; f) Y. Sugano, T. Yoshida, *Int. J. Mol. Sci*. **2021**, *22*, 5556.

[2] a) P. Nicholls, I. Fita, P. C. Loewen, *Adv. Inorg. Chem*. **2000**, *51*, 51–106; b) J. Vlasits, C. Jakopitsch, M. Bernroitner, M. Zamocky, P. G. Furtmüller, C. Obinger, *Arch. Biochem. Biophys*. **2010**, *500*, 74–81; c) A. Díaz, P. C. Loewen, I. Fita, X. Carpena, *Arch. Biochem. Biophys*. **2012**, *525*, 102–110; d) M. Alfonso-Prieto, P. Vidossich, C. Rovira, *Arch. Biochem. Biophys*. **2012**, *525*, 121–130; e) W. Hansberg, *Antioxidants* **2022**, *11*, 2173.

[3] a) S. C. Perry, D. Pangotra, L. Vieira, L.-I. Csepei, V. Sieber, L. Wang, C. Ponce de León, F. C. Walsh, *Nature Rev. Chem*. **2019**, *3*, 442–458; b) R. Ciriminna, L. Albanese, F. Meneguzzo, M. Pagliaro, *ChemSusChem*. **2016**, *9*, 3374-3381.

[4] a) S. Siahrostami, *ACS Energy Lett*. **2022**, *7*, 2717–2724; b) K. S. Exner, *Energy Adv*. **2023**, *2*, 522-529.

[5] a) M. Costas, M. P. Mehn, M. P. Jensen, L. Que Jr., *Chem. Rev*. **2004**, *104*, 939–986; b) M. M. Abu-Omar, A. Loaiza, N. Hontzeas, *Chem. Rev*. **2005**, *105*, 2227–2252; c) P. C. A. Bruijnincx, G. van Koten, R. J. M. Klein Gebbink, *Chem. Soc. Rev*. **2008**, *37*, 2716–2744; d) P. Comba, M. Kerscher, *Coord. Chem. Rev*. **2009**, *253*, 564–574; e) A. R. McDonald, L. Que Jr, *Coord. Chem. Rev*. **2013**, *257*, 414–428; f) W. Nam, Y.-M. Lee, S. Fukuzumi, *Acc. Chem. Res*. **2014**, *47*, 1146–1154; g) K. Ray, F. F. Pfaff, B. Wang, W. Nam, *J. Am. Chem. Soc*. **2014**, *136*, 13942–13958; h) L. Vicens, G. Olivo, M. Costas, *ACS Catal*. **2020**, *10*, 8611−8631; i) G. Mukherjee, J. K. Satpathy, U. K. Bagha, M. Q. E. Mubarak, C. V. Sastri, S. P. de Visser, *ACS Catal.* **2021**, *11*, 9761–9797.

[6] a) V. Balland, D. Mathieu, Y. M. N. Pons, J. F. Bartoli, F. Banse, P. Battioni, J.-J. Girerd, D. Mansuy, *J. Mol. Catal. A* **2004**, *215*, 81–87; b) J. Bautz, P. Comba, L. Que Jr, *Inorg. Chem*. **2006**, *45*, 7077–7082; c) M. J. Park, J. Lee, Y. Suh, J. Kim, W. Nam, *J. Am. Chem. Soc*. **2006**, *128*, 2630-2634; d) M. S. Seo, T. Kamachi, T. Kouno, K. Murata, M. J. Park, K. Yoshizawa, W. Nam, *Angew. Chem. Int. Ed*. **2007**, *46*, 2291–2294; e) J. A. Kovacs, L. M. Brines, *Acc. Chem. Res*. **2007**, *40*, 501–509; f) M. Martinho, P. Dorlet, E. Rivière, A. Thibon, C. Ribal, F. Banse, J.-J. Girerd, *Chem. Eur. J*. **2008**, *14*, 3182–3188 ; g) A. T. Fiedler, L. Que Jr, *Inorg. Chem*. **2009**, *48*, 11038–11047; h) J.-G. Liu, T. Ohta, S. Yamaguchi, T. Ogura, S. Sakamoto, Y. Maeda, Y. Naruta, *Angew. Chem. Int. Ed*. **2009**, *48*, 9262 –9267; i) P. Surawatanawong, J. W. Tye, M. B. Hall, *Inorg. Chem*. **2010**, *49*, 188–198; j) E. Nam, P. E. Alokolaro, R. D. Swartz, M. C. Gleaves, J. Pikul, J. A. Kovacs, *Inorg. Chem*. **2011**, *50*, 1592–1602; k) A. Thibon, V. Jollet, C. Ribal, K. Sénéchal-David, L. Billon, A. B. Sorokin, F. Banse, *Chem. Eur. J*. **2012**, *18*, 2715–2724; l) C. Wegeberg, F. R. Lauritsen, C. Frandsen, Steen Mørup, W. R. Browne, C. J. McKenzie, *Chem. Eur. J*. **2018**, *24*, 5134–5145; m) J. Serrano-Plana, F. Acuña-Parés, V. Dantignana, W. N. Oloo, E. Castillo, A. Draksharapu, C. J. Whiteoak, V. Martin-Diaconescu, M. G. Basallote, J. M. Luis, L. Que Jr., M. Costas, A. Company, *Chem. Eur. J*. **2018**, *24*, 5331–5340; n) C. Wegeberg, W. R. Browne, C. J. McKenzie, *ACS Catal*. **2018**, *8*, 9980−9991.

[7] a) A. K. Vardhaman, C. V. Sastri, D. Kumar, S. P. de Visser, *Chem. Commun*. **2011**, *47*, 11044–11046; b) Y. M. Kim, K.-B. Cho, J. Cho, B. Wang, C. Li, S. Shaik, W. Nam, *J. Am. Chem. Soc*. **2013**, *135*, 8838–8841; c) A. Thibon, J.-F. Bartoli, R. Guillot, J. Sainton, M. Martinho, D. Mansuy, F. Banse, *J. Mol. Catal. A* **2008**, *287*, 115–120 ; d) A. K. Vardhaman, P. Barman, S. Kumar, C. V. Sastri, D. Kumar, S. P. de Visser, *Chem. Commun*. **2013**, *49*, 10926–10928.

[8] A. S. Faponle, M. G. Quesne, C. V. Sastri, F. Banse, S. P. de Visser, *Chem. Eur. J*. **2015**, *21*, 1221–1236.

[9] A. Bohn, K. Sénéchal-David, J.-N. Rebilly, C. Herrero, W. Leibl, E. Anxolabéhère-Mallart, F. Banse, *Chem. Eur. J*. **2022**, *28*, e2022016.

[10] a) F. Buda, B. Ensing, M. C. M. Gribnau, E. J. Baerends, *Chem. Eur. J*. **2003**, *9*, 3436-3444; b) J. Chen, A. Draksharapu, D. Angelone, D. Unjaroen, S. K. Padamati, R. Hage, M. Swart, C. Duboc, W. R. Browne, *ACS Catal*. **2018**, *8*, 9665-9674; c) H.-Y. Chen, Y.-F. Lin, *J. Comput. Chem*. **2023**, *44*, 2058-2072.

[11] a) A. Ansari, A. Kaushik, G. Rajaraman, *J. Am. Chem. Soc*. **2013**, *135*, 4235–4249; b) L. V. Liu, S. Hong, J. Cho, W. Nam, E. I. Solomon, *J. Am. Chem. Soc*. **2013**, *135*, 3286–3299; c) A. S. Faponle, F. Banse, S. P. de Visser, *J. Biol. Inorg. Chem*. **2016**, *21*, 453–462; d) K. Cheaib, M. Q. E. Mubarak, K. Sénéchal-David, C. Herrero, R. Guillot, M. Clémancey, J.-M. Latour, S. P. de Visser, J.-P. Mahy, F. Banse, F. Avenier, *Angew. Chem. Int. Ed*. **2019**, *58*, 854–858; e) X. Cao, H. Song, X.-X. Li, Q.-A. Qiao, Y. Zhao, Y. Wang, *Dalton Trans*. **2022**, *51*, 7571–7580; f) C.-C. G. Yeh, T. Mokkawes, J. M. Bradley, N. E. Le Brun, S. P. de Visser, *ChemBioChem*. **2022**, *2022*, e202200257; g) Ü. İşci, A. S. Faponle, P. Afanasiev, F. Albrieux, V. Briois, V. Ahsen, F. Dumoulin, A. B. Sorokin, S. P. de Visser, *Chem. Sci*. **2015**, *6*, 5063–5075.

[12] a) P. Moënne-Loccoz, J. Baldwin, B. A. Ley, T. M. Loehr, J. M. Bollinger Jr, *Biochemistry* **1998**, *37*, 14659–14663; b) J. A. Broadwater, J. Ai, T. M. Loehr, J. Sanders-Loehr, B. G. Fox, *Biochemistry* **1998**, *37*, 14664-14671.

[13] a) P. E. M. Siegbahn, *Philos. Trans. R. Soc. Lond. B Biol. Sci.* **2008**, *363*, 1221-1228; b) M. Retegan, V. Krewald, F. Mamedov, F. Neese, W. Lubitz, N. Cox, D. A. Pantazis, *Chem. Sci*. **2016**, *7*, 72-84; c) V. A. Larson, B. Battistella, K. Ray, N. Lehnert, W. Nam, *Nature Rev. Chem*. **2020**, *4*, 404–419.

[14] a) I. Prat, A. Company, V. Postils, X. Ribas, L. Que Jr., J. M. Luis, M. Costas, *Chem. Eur. J*. **2013**, *19*, 6724–6738; b) I. Prat, J. S. Mathieson, M. Güell, X. Ribas, J. M. Luis, L. Cronin, M. Costas, *Nature Chem*. **2011**, *3*, 788–793.

[15] a) X.-X. Li, V. Postils, W. Sun, A. S. Faponle, M. Solà, Y. Wang, W. Nam, S. P. de Visser, *Chem. Eur. J*. **2017**, *23*, 6406–6418 ; b) S. Ghafoor, A. Mansha, S. P. de Visser, *J. Am. Chem. Soc*. **2019**, *141*, 20278–20292; c) E. F. Gérard, V. Yadav, D. P. Goldberg, S. P. de Visser, *J. Am. Chem. Soc*. **2022**, *144*, 10752−10767.

[16] *Gaussian*-09, Revision D.01, M. J. Frisch, G. W. Trucks, H. B. Schlegel, G. E. Scuseria, M. A. Robb, J. R. Cheeseman, G. Scalmani, V. Barone, B. Mennucci, G. A. Petersson, H. Nakatsuji, M. Caricato, X. Li, H. P. Hratchian, A. F. Izmaylov, J. Bloino, G. Zheng, J. L. Sonnenberg, M. Hada, M. Ehara, K. Toyota, R. Fukuda, J. Hasegawa, M. Ishida, T. Nakajima, Y. Honda, O. Kitao, H. Nakai, T. Vreven, J. A. Montgomery, Jr., J. E. Peralta, F. Ogliaro, M. Bearpark, J. J. Heyd, E. Brothers, K. N. Kudin, V. N. Staroverov, T. Keith, R. Kobayashi, J. Normand, K. Raghavachari, A. Rendell, J. C. Burant, S. S. Iyengar, J. Tomasi, M. Cossi, N. Rega, J. M. Millam, M. Klene, J. E. Knox, J. B. Cross, V. Bakken, C. Adamo, J. Jaramillo, R. Gomperts, R. E. Stratmann, O. Yazyev, A. J. Austin, R. Cammi, C. Pomelli, J. W. Ochterski, R. L. Martin, K. Morokuma, V. G. Zakrzewski, G. A. Voth, P. Salvador, J. J. Dannenberg, S. Dapprich, A. D. Daniels, O. Farkas, J. B. Foresman, J. V. Ortiz, J. Cioslowski, D. J. Fox, Gaussian, Inc., Wallingford CT, 2010.

[17] a) A. D. Becke, *J. Chem. Phys*. **1993**, *98*, 5648–5652; b) C. Lee, W. Yang, R. G. Parr, *Phys. Rev. B* **1988**, *37*, 785–789.

[18] S. Grimme, J. Antony, S. Ehrlich, H. Krieg, *J. Chem. Phys*. **2010**, *132*, 154104.

[19] C. Adamo, V. Barone, *J. Chem. Phys*. **1999**, *110*, 6158–6169.

[20] a) R. A. Kendall, T. H. Dunning Jr, R. J. Harrison, *J. Chem. Phys*. **1992**, *96*, 6796–6806; b) W. J. Hehre, R. Ditchfield, J. A. Pople, *J. Chem. Phys*. **1972**, *56*, 2257–2261; c) M. M. Francl, W. J. Pietro, W. J. Hehre, J. S. Binkley, M. S. Gordon, D. J. DeFrees, J. A. Pople, *J. Chem. Phys*. **1982**, *77*, 3654–3658.

[21] J. Tomasi, B. Mennucci, R. Cammi, *Chem. Rev*. **2005**, *105*, 2999–3009.

[22] a) A. V. Marenich, J. Ho, M. L. Coote, C. J. Cramer, D. G. Truhlar, *Phys. Chem. Chem. Phys*. **2014**, *16*, 15068-15106; b) E. McCafferty, *Introduction to Corrosion Science*, Springer Publishers, New York, 2010.

[23] a) F. G. Cantú Reinhard, A. S. Faponle, S. P. de Visser, *J. Phys. Chem. A* **2016**, *120*, 9805–9814; b) F. G. Cantú Reinhard, M. A. Sainna, P. Upadhyay, G. A. Balan, D. Kumar, S. Fornarini, M. E. Crestoni, S. P. de Visser, *Chem. Eur. J*. **2016**, *22*, 18608–18619; c) H. P. H. Wong, T. Mokkawes, S. P. de Visser, *Phys. Chem. Chem. Phys*. **2022**, *24*, 27250–27262; d) H. S. Ali, J. Warwicker, S. P. de Visser, *ACS Catal*. **2023**, *13*, 10705–10721.

[24] a) S. F. Nelsen, M. J. R. Yunta, *J. Phys. Org. Chem*. **1994**, *7*, 55-62; b) F. Guo, L. Chai, S. Zhang, H. Yu, W. Liu, K. P. Kepp, L. Ji, *Environ. Sci. Technol*. **2020**, *54*, 2902−2912.

[25] L. Ji, J. Zhang, W. Liu, S. P. de Visser, *Chem. Asian J.* **2014**, *9*, 1175–1182.

Entry for the Table of Contents:

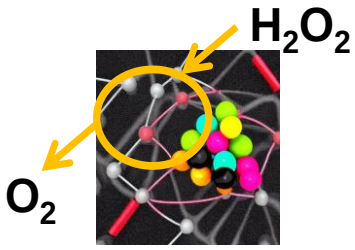

Text for Table of Contents: Density functional theory studies on the reduction of H_2O_2 on a nonheme iron center is shown to lead to dioxygen products efficiently through the formation of a μ-1,2-peroxo bridged diiron(III)dihydroxo complex from two iron(IV)-oxo(hydroxo) intermediates.

Institute and/or researcher Twitter usernames: The University of Manchester (@OfficialUoM); Department of Chemical Engineering (@UoMSciEng); Manchester Institute of Biotechnology (@UoMMIB). Henrik PH Wong (@HenrikPHWong)